Red Tide Detection Based on Improved DenseNet Network—Example of Red Tide Detection from Geostationary Ocean Color Imager Data in Bohai Sea

Yanling Han, Xuewei Liu, Zhenling Ma,* Yun Zhang, Ruyan Zhou, and Jing Wang

Shanghai Ocean University, 999 Huchenghuan Road, Pudong New Area, Shanghai 201308, China

The effective and rapid detection of red tide has significant research implications in China's offshore regions, where severe seawater eutrophication leads to frequent red tide events. With the rapid development and widespread application of remote sensing and deep learning technologies, the technical means for high-performance, large-scale red tide detection are now available. In this paper, aiming at solving the problems of limited number of samples in red tide detection and the limited improvement of red tide detection accuracy based on traditional methods, we propose a red tide detection method based on improved DenseNet, which uses dense convolutional blocks and neighborhood space features to extract information at different levels and scales, makes full use of and integrates underlying boundary details and high-level semantic information, and solves the problem of limited improvement of detection accuracy caused by a small number of samples and an unbalanced sample distribution. At the same time, through the attention mechanism based on the squeeze-and-excitation (SE) module, feature weighting optimization is carried out for the bands conducive to red tide detection, which can further improve the detection accuracy. To verify the effectiveness of this method, we use Geostationary Ocean Color Imager (GOCI) data of the red tide that occurred in the Bohai Sea in 2014 in our experiment. The experimental results show that the proposed method achieves better red tide detection (overall classification accuracy: 98.03%) than state-of-the-art red tide detection methods and is more suitable for red tide detection by remote sensing.

1. Introduction

In recent years, with the rapid economic development of the Bohai Sea region and the overexploitation of marine resources,[1,2] the ecological conditions of the Bohai Sea have been severely damaged by the deteriorating quality of water bodies, the severe eutrophication of seawater, and frequent red tide disasters. Statistical analysis by Song *et al.* showed that between 1954 and 2016, there were a total of 189 red tides in the Bohai Sea, 21 of which had a surface area of over 1000 km^2.[3] The red tide frequency in the Bohai Sea has increased significantly

since 2000, and the red tide has gradually expanded from small, sporadically distributed areas to patches of sea.[4,5] The main period of red tide in the Bohai Sea is from May to August. The waters of Tianjin and Qinhuangdao and the western waters of Liaodong Bay are areas of frequent red tides. In particular, the red tide that occurred in the waters of Qinhuangdao in 2014 had a duration of 85 days and not only caused enormous losses to the local mariculture industry, but also impacted the local fisheries and marine products. Therefore, the effective monitoring and timely observation of red tide are essential for a healthy ecological environment.[6]

The monitoring of red tide, as well as the investigation of the initial and outbreak conditions, is crucial for its early warning and prediction.[7] Important tasks in marine ecological monitoring are to monitor red tide and determine the environmental status of the area of red tide occurrence and its changes over time, which can provide a scientific basis for coastal local governments to reduce the damage that red tide causes to the coastal marine economy. The earliest monitoring of red tide was based on visual observation and the sampling of seawater that was taken to the laboratory for the analysis of various indicators and comparison with their thresholds. Although this approach is accurate in determining the condition of the sampling point, this method is limited in that it can only determine the red tide condition of the sampling point at the time of sampling. It is also time-consuming and costly. Over the past few years, the development of remote sensing technology has provided a new, more macroscopic and effective means of monitoring red tide.[8,9] Satellite remote sensing for the extraction of red tide information focuses on the biological and environmental conditions under which the red tide is occurring.[10–12] By correcting, synthesizing, analyzing, and interpreting satellite imagery, the results of processing can be analyzed to understand red tide characteristics and to estimate red tide information such as the extent, range, and general trend of development of red tide, providing an important means for rapidly synchronized, spatially extensive, and high-frequency continuous monitoring of red tide.[13]

There are three main classes of methods using satellites to detect red tide. The first class involves the identification of red tide through parameters such as chlorophyll content and temperature.[14,15] Jiang and Zhang used chlorophyll concentration and ERGB effects to analyze Bohai Sea red tide by visual discrimination in 2018.[16] The second class of methods uses remote sensing to detect the significant spectral features of the water mass at the time of red tide, such as strong reflection near the band of green light (550 nm). The spectral characteristics of the water body change accordingly when red tide organisms congregate in large numbers and the color of the water body changes.[17,18] Jiang *et al.* obtained the normalized off-water Geostationary Ocean Color Imager (GOCI)-nLw emissivity (550 nm) by quick atmospheric correction and used nLw (555 nm) as the characteristic band to obtain information on red tide.[19] The third class is red tide detection by algal fluorescence;[20] some algae appear fluorescent in the red-light band. Feng *et al.* used the fluorescence line height of different water bodies to extract the red tide index to determine the state of the water body.[21] The main sensors currently in use include the Moderate Resolution Imaging Spectroradiometer (MODIS), Sea-Viewing Wide Field-Of-View Sensor (SeaWIFS), Medium Resolution Imaging Spectrometer (MERIS), and GOCI. GOCI can acquire eight scenes with a time interval of 1 h per day, which is different from the traditional polar-orbiting satellite, which can only pass through a scene once per day.

This makes it possible to monitor changes in the marine environment and marine disasters by remote sensing on a time-by-time basis.

Over the past few years, with the development of deep learning, an increasing number of researchers have begun to use deep learning to detect red tides.[22–25] In 2019, Kim *et al.* proposed a U-Net network for a study related to the detection of red tide using GOCI data from the waters surrounding the Korean Peninsula. U-Net is a U-shaped convolutional neural network (CNN) with an encoder and decoder structure, which is widely used for pixel classification or target segmentation.[26] In the same year, Lee *et al.* developed a novel red tide detection scheme for the southern coast of the Korean Peninsula based on deep learning and satellites with high spatial and temporal resolution.[27] In 2021, Shin *et al.* developed a U-Net deep learning model based on PlanetScope for detecting red tide on the southern coast of Korea and obtained better results than those of the traditional red tide index method by controlling the proportion of red tide images and non-red-tide images in different training sets.[28] Despite the good detection accuracy of the above experiments, further improvements in red tide detection accuracy are limited by the small sample size and imbalanced sample distribution due to the infrequently measured data. In addition, there is still much room for improvement in the detailed extraction of the red tide boundary.

Referring to the above research, in this paper, we propose a red tide detection model called RT-DenseNet (RedTide-DenseNet) based on an improved DenseNet network. To extract features of different levels and scales from a relatively small amount of red tide image data and improve the detection of target points, we use the spatial features of dense blocks and convolutional neighborhoods to improve the utilization of red tide image information by fully mining the image features around the target detection point and fusing it with the information of the underlying details. We also solve the problem of the limited improvement of detection accuracy due to the small amount of data at the target point and the unbalanced sampling distribution. In addition, we analyze the effect of different numbers of bands on the detection, and we use the focus mechanism based on the squeeze-and-excitation (SE) module to optimize the feature weights of each band in the red tide images, thus extracting band information that may better reflect the red tide phenomenon and further improving the red tide detection accuracy.

Section 2 deals with the preprocessing of experimental data and the production of datasets, Sect. 3 explains the reasons for choosing the DenseNet network and the proposed new network, and Sect. 4 describes the experimental design environment, the analysis of parameters, and the analysis of results.

2.　Data and Processing Methods

2.1　Study region

The Bohai Sea is located at 37°07′–41°00′N, 117°35′–122°16′E. It is surrounded by land on three sides and consists of five parts: Liaodong Bay, Laizhou Bay, Bohai Strait, Bohai Bay, and the central sea. It has an area of about 77000 km^2, a coastline of about 3800 km, and an average depth of 18 m. It is the only semi-enclosed inland sea in China. The Bohai Sea has poor water

exchange capacity, dilution capacity, and diffusion capacity, as well as many rivers along the coast. The rivers flow through the surrounding three provinces and one city. The coastal areas are economically developed and intensively used, and the rivers carry large amounts of industrial, domestic, and agricultural sewage, the latter resulting from the excessive application of agricultural fertilizers, directly into the Bohai Sea, leading to a decline in the water quality and eutrophication in the Bohai Sea and frequent red tide disasters. According to *China Marine Environmental Quality Bulletin*, offshore water pollution in the Bohai Sea is severe. The water fails to meet the standards for inorganic nitrogen, active phosphate, and other substances.

2.2 Experimental data

GOCI is a next-generation ocean water color imager developed in Korea and is carried on the Communication, Ocean, Meteorological Satellite (COMS), the first geostationary meteorological satellite launched in Korea in 2010. GOCI covers an area of 2500 km × 2500 km with 500 m spatial resolution and has very high temporal resolution, providing observations at eight time points per day from 8:30 to 15:30 daily at hourly intervals. It has a spectral resolution of 402–885 nm and contains eight bands of data in total. GOCI data can be divided into L1B data, L2 data, and L3 data in accordance with the class.

For this experiment, we use data from red tide hazard information published in *China Marine Bulletin*, and the single largest area of red tide caused by the inhibition of feeding golden coccolithophorids occurred in the nearshore waters of Qinhuangdao during the period from 15 May to 7 August 2014. We use this red tide disaster as the subject of this paper, and the L1B level data of GOCI was selected, as shown in Fig. 1. From the true color image map, we filtered out the data with less cloud cover during the red tide outbreak in the Bohai Sea and finally selected the data of 28 May. To obtain the reflectance data from GOCI, the Geographic Lat/Lon projection was used to generate the required Geographic Lookup Table (GLT) file from the
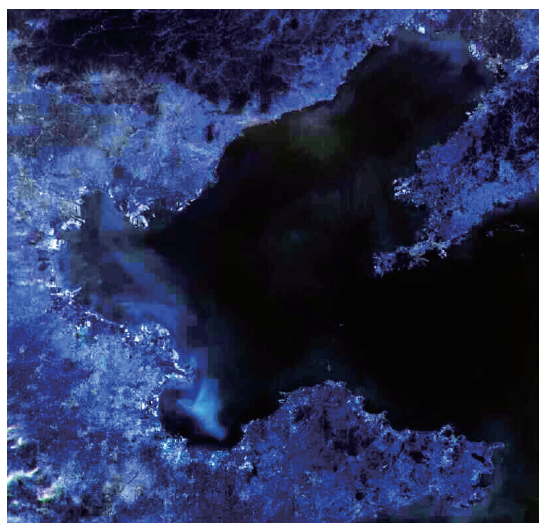

Fig. 1.   (Color online) Region chosen for the experimental data: the Bohai Sea.

latitude and longitude information included with GOCI, and the data were geometrically corrected for the GLT using ENVI software. Atmospheric corrections were made using the SeaDas built-in atmospheric correction method for GOCI data, officially published by NASA Ocean Biology Processing Group (OBPG).

2.3   Dataset generation

For the labeling of the dataset, we first extracted the chlorophyll concentration products using the official GOCI Data Processing System (GDPS) software provided by GOCI. We then determined a suitable threshold to match the area of red tide occurrence in the images with the area information provided in the 2014 *China Marine Bulletin*. The L2A chlorophyll product data obtained from the GOCI data were visually displayed, as illustrated in Fig. 2. When selecting the detailed area of GOCI data, because of the presence of land and cloud cover, no data were available. We selected nine areas of size 256×256 from the remote sensing data obtained at five times (09:30, 10:30, 11:30, 12:30, and 13:30) on 28 May 2014. Given the sample budget, the ratio of pixel locations within the overall selected range of red tide area to the normal sea area is close to one. Lastly, the remote sensing data at 14:30 were taken for model validation and the visualization of results for comparative purposes.

A suitable size for segmenting remote sensing data was selected before the image was input to the network, and in the following experimental validation, the image was ultimately segmented into a 27×27 block of images, with the center pixel point used as a sample label depending on whether red tide occurs. At this point, part of the data still contained cloud-obscured data-free pixel points, which would adversely affect the classification results of neighboring pixels. In cases with a small amount of missing data, we used interpolation to add missing data as needed. Interpolation is an important method for approximating discrete
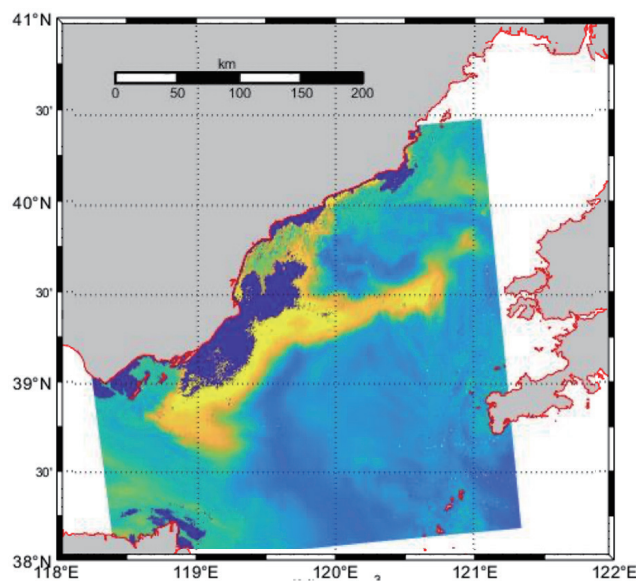

Fig. 2.   (Color online) Result of visualizing the chlorophyll concentration product of the GOCI data.

functions and is used to estimate the approximate value of a function at an arbitrary point using the values of the function at a finite number of points. It can be used to fill in the gaps between pixels when transforming an image to avoid the effect of dirty data on experimental results. In the case of a small amount of missing data, we extracted the points adjacent to the missing part to establish a coordinate system and used the boundary points at the ends of the horizontal and vertical coordinates as reference points to supplement the missing data by interpolation. In the case of too much missing data, we discarded blocks of images directly to reduce their impact on model training. The total amount of data obtained after interpolation to generate missing data is shown in Table 1.

Because the red tide index calculation is primarily influenced by the first four bands, to determine whether the other two bands affect red tide detection, two sets of GOCI datasets containing different bands were constructed by cropping the spectral dimensions. One set contained only wavelengths from one to four bands, including the main bands such as the blue and green bands, which are mainly affected by the occurrence of red tide. The other set contained the six available bands from the GOCI dataset and was used to compare the classification results of datasets in the two different bands.

3. Model Design

3.1 Overall framework of model

The general framework for the proposed method is shown in Fig. 3. It is divided into three main modules: the data entry module, the feature extraction module, and the classification

Table 1
Data set after adding missing data.

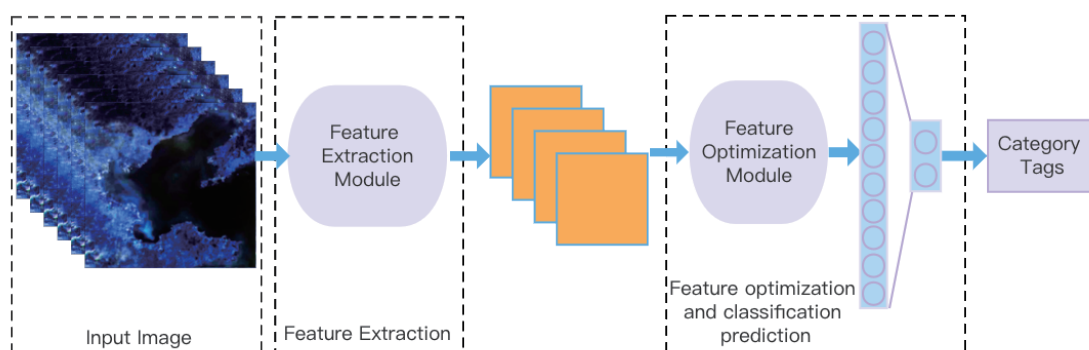|	Normal seawater	Red tide	Total
Training data	13205	12286	25491
Test data	316942	110576	427518
Total	330147	122862	453009

Fig. 3.　(Color online) Overall framework of the model.

module. In the data input module, we first preprocess the GOCI data, then select the pixel blocks within a certain neighborhood around the pixel point selected as the center of the input data. To extract features at different levels and scales across densely connected blocks, the feature extraction module is executed by the enhanced DenseNet model. The final classifier consists of the enhanced DenseNet, the SE module, and a fully connected network with a SoftMax activation function.

3.2   Extraction of red tide features based on enhanced DenseNet

In a CNN, the relationship between the layers of the network is usually determined by batch normalization (BN), rectified linear units (ReLU), convolutional layers (Conv), and dropout layers. Experimental studies have shown that a more accurate and efficient network model can be obtained if a more direct connection is made between the initial input layer of the CNN and the final output layer. DenseNet performs a more aggressive dense binding than ResNet. ResNet links each layer to previous layers (typically two or three layers) through a form of summation at the element level, whereas in DenseN*et all* layers are connected to each other in a way that ensures maximum information flow between the layers in the network.

$$X_l = H_l\left(\left[X_0, X_1, X_2, \ldots, X_{l-1}\right]\right) \tag{1}$$

Unlike ResNet, DenseNet links features extracted from each layer together to achieve feature reuse. Each layer takes as its input the feature maps from all previous layers, whereas its own feature maps serve as the input to all subsequent layers. As shown in Eq. (1), in a traditional CNN with L layers, there are L connections, one between each layer and its successor, whereas DenseNet has $L(L+1)/2$ connections. To maintain feed-forward functionality, each layer receives additional input from all previous layers and passes its own feature map to all subsequent layers. Because of this connection, the gradients of the loss function and the original input signal are directly available to each layer of the network, which leads to an implicitly deep level of supervision. This approach encourages the reuse of shallow features throughout the network and effectively mitigates the gradient vanishing problem that tends to arise in CNNs, making it more amenable to training deeper networks. This allows the extraction of a wide variety of feature images from different levels of remotely sensed data. During red tide detection, it is difficult to distinguish the red tide, because the difference between the detection points at the bounding part is small, whereas DenseNet can extract a larger number of feature images around the detection points and determine if the red tide is occurring at the detection points by judging the change in water quality around them.

The RT-DenseNet model proposed in this paper is composed of SE, BN, ReLU, Conv, and dropout layers. Compared with the original network, the SE module is added to each RT-Dense block and each transition layer. In this way, attention weights are added to the different channels to obtain better red tide monitoring performance, as shown in Fig. 4.
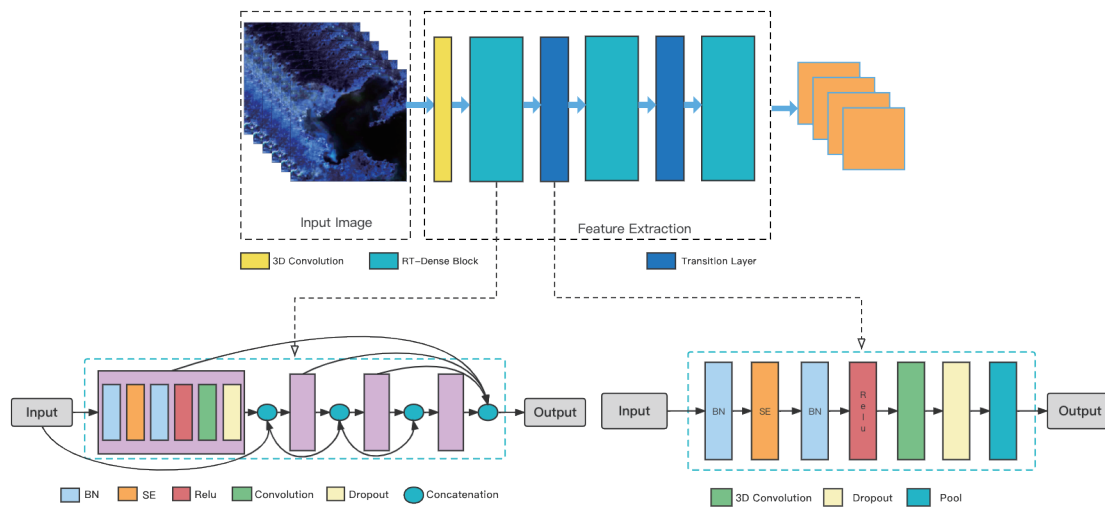
Fig. 4.   (Color online) Feature extraction module.

3.3   Feature optimization based on SE module

Studies have shown that red tide can only occur in waters with a high chlorophyll content and does not occur in waters with a low chlorophyll content. Red tide is often accompanied by an increase in water column chlorophyll content, and as the amount of chlorophyll in the water column increases, the data in the blue-green band in the remotely sensed images undergoes relatively large changes. The different degrees of data variation in different bands mean that the degree of influence of data in different bands may differ for red tide detection. Assigning different weights in accordance with the degree of influence in different bands can improve the classification accuracy of the detection model.

The pooled convolution process in the training of traditional network models is usually based on the default assumption that each channel in the feature map has the same weight, but in practice, different channels in the feature map have different degrees of influence on the feature extraction, and if every channel has the same weight, then some degree of loss will occur. The SE module is proposed as a solution to this problem.

We assume that we are inputting a feature map of size $H \times W \times C$. By first performing an overall pooling operation (pooling size $H \times W$), we can obtain a characteristic map of size $1 \times 1 \times C$. In this case, there are two fully connected layers, and the number of neurons in the first fully connected layer is C/R. This pooling operation is therefore a method of dimensionality reduction. The second fully connected layer is again dimensioned up to C neurons. The advantage of this is that more nonlinear processing is added to adjust for complex correlations between channels. A sigmoid layer is then added to obtain features of size $1 \times 1 \times C$, and finally, an operation of complete multiplication is performed on the original feature maps of sizes $H \times W \times C$ and $1 \times 1 \times C$. After increasing the attention weights, the feature map can be obtained by performing a full multiplication of the feature map. This construction is illustrated in Fig. 5.
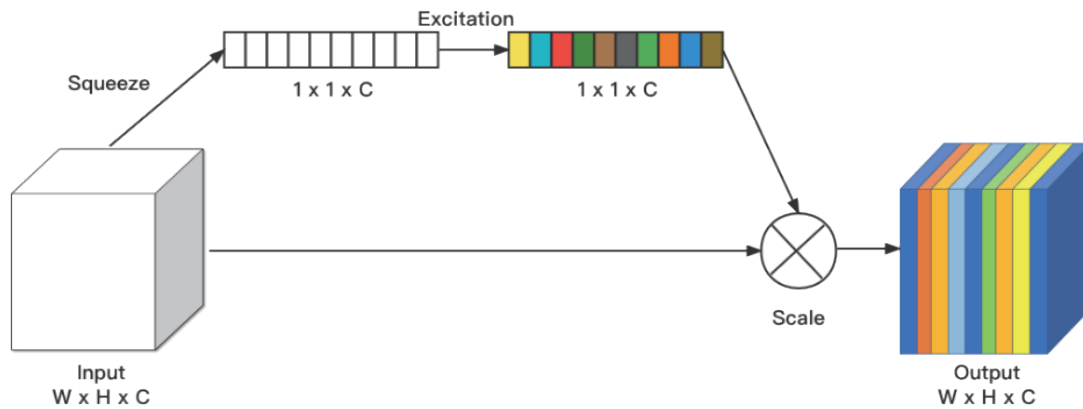
Fig. 5. (Color online) SE module.

4. Experimental Results and Analysis

4.1 Experimental setup

To test the feasibility of our proposed experimental approach, we use some evaluation methods such as overall classification accuracy (OA), the accuracy of each category, and the Kappa coefficient. For the experiment, we used a Python-based implementation of the TensorFlow framework. The Adam algorithm was used to optimize the proposed model, and the learning rate, batch size, dropout rate, and number of trainings were 0.00001, 200, 0.5, and 5000, respectively. The experimental hardware comprised an Intel i7-11700 core, a 2.50 GHz processor, and 16 GB RAM.

The classification accuracy of the network model is primarily determined by the structure of the deep learning network. We designed an RT-DenseNet network for GOCI feature extraction. Once the data features have been extracted through the model network, the extracted features are fed to the classification layer for classification. Table 2 shows the details of the lattice model in the experiment, where CONV_3 × 3 × 3 refers to a 3D convolution with a convolution kernel size of 3 × 3 × 3 and 24 refers to the dimensionality of the output feature map, whose detailed structure is given in Table 3.

4.2 Analysis of model parameters

The size of the input image is one of the important factors affecting the classification of CNNs. In this study, the effect of input images of different scales on the classification results of the network was tested separately while the other parameters were kept the same. As shown in Table 4, the OA of the model improved from 95.40 to 98.03% for six-band data and from 85.80 to 87.30% for four-band data as the scale of the input images gradually increased from 21 × 21 to 27 × 27. The overall classification performance of the model increases with the scale of the input images for both types of data, indicating that the increase in data volume allows the network to extract more effective features from the data and obtain better classification results. However, as

Table 2
RT-DenseNet classification network structure.

Layer	Number of features
CONV_3 × 3 × 3	24
RT-DenseNet-Layer	36
RT-DenseNet-Layer	48
RT-DenseNet-Layer	60
RT-DenseNet-Layer	72
CONV_1 × 1 × 1	36
Avg Pool_2 × 2 × 2	36
RT-DenseNet-Layer	48
RT-DenseNet-Layer	60
RT-DenseNet-Layer	72
RT-DenseNet-Layer	84

Table 3
Details of the RT-DenseNet layer structure.

	SE-Layer
	BN
	ReLU
RT-DenseNet layers	CONV_3D_5 × 5 × 5
	BN
	ReLU

Table 4
Effect of input image size on classification accuracy.

Input image size	Six-band data		Four-band data	
	OA (%)	Kappa × 100	OA (%)	Kappa × 100
21 × 21	95.40	95.21	85.80	85.14
23 × 23	96.93	96.34	86.43	86.42
25 × 25	97.00	97.35	86.67	86.11
27 × 27	98.03	98.42	87.30	86.69
29 × 29	97.23	97.05	85.36	86.02

the size of the input images continues to increase, the OA of the model decreases from 98.03 to 97.23% for the six-band data and from 87.30 to 85.36% for the four-band data. The overall classification performance of the model starts to decrease for both types of data, indicating that the data in the added range may not be the same type of data as the central data as the size increases, which in turn affects the classification results for the central pixel points. Therefore, in our subsequent experiments, a data block of size 27 × 27 was used as the model input data.

The convolution operation was performed on the input image to extract its features. An appropriate convolution kernel size can extract the image features more effectively, which is an important means of improving the classification accuracy of neural networks. In this paper, we compare the effect of convolutional kernel sizes of 3 × 3, 5 × 5, and 7 × 7 on the classification accuracy of the model while keeping the other parameters the same. As can be seen from the experimental results in Table 5, the OA of the four-band data increased from 85.10 to 87.30% and the OA of the six-band data increased from 95.73 to 98.03% when the convolution kernel size increased from 3 × 3 to 5 × 5. However, the OA of the four-band data and six-band data tends to decrease as the size of the convolutional kernel is increased to 7 × 7. This indicates that the classification accuracy of the model does not increase with the convolutional kernel size, and when the number of parameters reaches a certain level, the excessive number of parameters adversely affects the classification results of the model. In our subsequent experiments, a convolutional kernel of size 5 × 5 was used.

The growth rate, which determines the number of feature maps obtained from each feature extraction, is an important parameter in the DenseNet network not only to improve the accuracy

Table 5
Effect of convolution kernel size on classification accuracy.

Convolution kernel size	Six-band data		Four-band data	
	OA (%)	Kappa × 100	OA (%)	Kappa × 100
3 × 3	95.73	93.73	85.10	83.16
5 × 5	98.03	98.42	87.30	86.69
7 × 7	94.86	92.85	84.00	82.65

Table 6
Effect of growth rate on classification accuracy.

Growth rate	Six-band data		Four-band data	
	OA (%)	Kappa × 100	OA (%)	Kappa × 100
8	96.13	96.69	85.80	84.96
10	96.87	98.01	86.33	85.78
12	98.03	98.42	87.30	86.69
14	96.86	97.82	85.93	85.01

of model classification, but also to optimize the number of parameters and the computation of the model. We next compare the classification performance of the model at different growth rates while keeping the other parameters the same. As shown in Table 6, when the growth rate is set to 12, the classification accuracy of the six-band data model is 98.03% and the classification accuracy of the four-band data model is 87.30%, which were the highest accuracies obtained among the growth rates tested. The growth rate was thus set to 12 in the subsequent experiments.

4.3 Experimental results and analysis

4.3.1 Comparative analysis of proposed method and other methods

To verify the feasibility of the proposed RT-DenseNet network for red tide detection using GOCI data, we used a variety of learning methods for comparison.

First, for the traditional machine learning method, we transformed the 4D data used in the experiment into 2D data. We then input the data to the SVC binary classifier and obtained *TP* (correctly predicted as positive samples), *FP* (incorrectly predicted as positive samples), *TN* (correctly predicted as negative samples), and *FN* (incorrectly predicted as negative samples) using the accuracy calculation formula

$$P = \frac{TP}{TP + FP}. \tag{2}$$

P represents the classification accuracy of the experiment, and the classification accuracy of the SVC binary classifier is 86.39%.

We then split the same training data into images of appropriate sizes for the U-Net network and the original DenseNet network in accordance with the characteristics of the different networks. By comparing the classification results of each experiment, as shown in Table 7, we found that, compared with the traditional machine learning method, the U-Net network can

Table 7
Overall accuracy of SVM, U-Net, DenseNet, and RT-DenseNet.

Method	OA (%)	Kappa × 100
SVM	86.39	85.78
U-Net	93.87	93.67
DenseNet	95.67	95.87
RT-DenseNet	98.03	98.42

extract deeper features, the weight sharing makes the model simpler, and the generalization ability increases. The resulting model classification accuracy is 93.87%, and the classification performance in red tide detection from remotely sensed images is clearly much better than that in the traditional machine learning method. Compared with the traditional CNN, the DenseNet network can achieve better classification results with the same number of parameters. This is because the DenseNet network more strongly integrates the depth features by the intensive connection of features at different levels and improves the utilization of features while mitigating the vanishing-gradient phenomenon and increasing the anti-fitting performance of the network. The OA of the model is 95.67%.

Since the change in the value of each band in remote sensing data at the occurrence of red tide is different, the spectral values of the blue and green bands tend to fluctuate widely because of the large number of algae in the water body at the occurrence of red tide. The different importances of different channels lead to different degrees of reflection upon the change in red tide for different spectral channels. To address this problem, we propose an improved RT-DenseNet for DenseNet in this paper, make use of the different contributions of different channels to red tide detection to perform a weighted optimization, and distinguish the effectiveness of red tide detection of different feature maps in convolution pooling to achieve feature enhancement. After adjusting the relevant parameters, the OA of the model was 98.03%, an improvement of 2.36 percentage points relative to the original DenseNet network, indicating a significant improvement in the classification results of red tide.

4.3.2 Visualization results of red tide detection by proposed method

4.3.2.1 Assessment methods

To test the classification performance of the RT-DenseNet network model, we used a more general framework, forecast validation, that can be implemented with four different types of probabilities. Two methods commonly used in statistics, the probability of detection (POD) and false alarm ratio (FAR), were used. In this experiment, *POD* indicates the percentage of pixels covered by red tide that are detected as red tide:

$$POD = p(d=1 \mid x=1) = \frac{p(d=1, x=1)}{p(x=1)}.$$

(3)

FAR indicates the percentage of false detections where the original pixel is a normal sea area among all pixel points where the detection result is red tide:

$$FAR = p(x = 0 | d = 1) = \frac{p(d = 1, x = 0)}{p(d = 1)}. \tag{4}$$

POD_{NO} indicates the correct recognition rate of the original data as pixel points in normal sea:

$$POD_{NO} = p(d = 0 | x = 0) = \frac{p(d = 0, x = 0)}{p(x = 0)}. \tag{5}$$

The larger the *POD* and the smaller the *FAR*, the better the model classification.

4.3.2.2 Comparison of results

On the basis of the results of the several previous comparisons and validations, we trained the network with the optimal parameters and obtained the optimal classification model. We then used the GOCI remote sensing data at 14:30 on May 28, 2014, which was segmented according to the 27 × 27 specification and input to the model to obtain the model prediction results for the real data. The prediction accuracy for each method is shown in Table 8.

The prediction results are visualized in Fig. 6. Figure 6(a) shows the actual red tide occurrence area and Fig. 6(e) shows the red tide area predicted by the RT-DenseNet model. The size of the GOCI remote sensing data at 14:30 used for the prediction was 365 × 426, the selected area has little cloud coverage, the dark blue part in Fig. 6(a) is the cloud coverage area, the yellow part in each figure is the area where red tide is predicted to occur, and the cyan part is the normal sea area where red tide is predicted not to occur. The prediction accuracy for positive samples reached 95.11% for *POD*, 97.35% for POD_{NO}, and 9.63% for *FAR*. The obtained accuracy and the visualization results show that the proposed method can obtain better red tide monitoring results than the other methods. In particular, in the identification of boundary data, we mark the boundary part of the data and compare it with the data after prediction by each method. We found that RT-DenseNet had the highest classification accuracy among the methods of up to 92.36%; thus, the boundary data classification performance was improved.

Table 8
Prediction accuracy for each method.

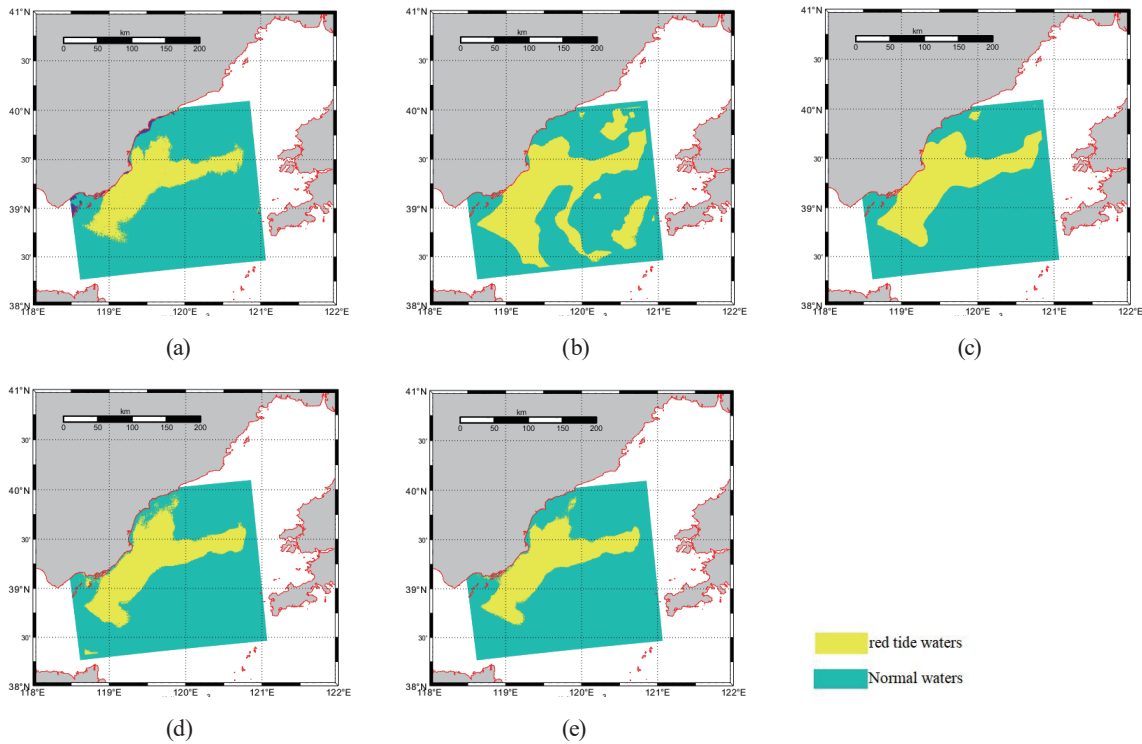| Method	*POD* (%)	POD_{NO} (%)	*FAR* (%)
SVM	88.29	81.29	20.36
U-Net	91.80	89.60	15.68
DenseNet	93.83	93.63	13.48
RT-DenseNet	95.11	97.35	9.63

Fig. 6.   (Color online) Actual red tide area and prediction results. (a) Actual range, (b) SVM, (c) U-Net, (d) DenseNet, (e) RT-DenseNet.

5.   Conclusions

To further improve the accuracy of red tide detection by remote sensing, we designed an improved DenseNet model. DenseNet can mine the depth features of red tide images through dense connectivity, enabling the effective use of multilevel features. By adding an attention mechanism to the DenseNet network, different feature maps are weighted and optimized to further mine the red tide boundary features, thus achieving the fine detection of red tide boundary areas and improving red tide detection accuracy. We segmented the red tide image of 28 May 2014 in the Bohai Sea into 27 × 27 images and created four-band and six-band datasets to compare the effect of different numbers of bands on the experimental results. The data sets were fed into the network for training, and the experimental results showed that the six-band data set had the better accuracy with an OA of 98.03% and an edge classification accuracy of 92.36%. We also compared the detection results obtained from different models and visualized them. The experimental results show that the proposed method achieves better detection results and has more accurate performance in boundary detection than the traditional network model. Furthermore, we also analyzed in detail the effects of different parameters, including the input image size, the size of the convolution kernel, and the feature learning rate, on the detection performance of the model. This study provides a new method and idea for red tide detection using optical remote sensing data.

Acknowledgments

References

1   S. Zhang, X. Wang, C. Guan, X. Shen, and R. Li: Acta Scientiarum Naturalium Universitatis Pekinensis **56** (2020). https://doi.org/10.13209/j.0479-8023.2020.110
2   Y. Dou, J. Shang, P. Shao, J. Gao, X. Jia, and W. Zhou: J. Hydroecol. **41** (2020). https://doi.org/10.15928/j.1674-3075.2020.06.017
3   N. Song, N. Wang, N. Wu, and W. Lin: Chin. Environ. Sci. **38** (2018). https://doi.org/10.19674/j.cnki.issn1000-6923.2018.0136
4   B. Wang, J. Cui, L. Li, H. Shi, J. Wang, and C. Liu: Marine Environ. Sci. **40** (2021). https://doi.org/10.13634/j.cnki.mes.2021.02.006
5   Z. Yu and N. Chen: Oceanologia Et Limnologia Sinica **50** (2019). https://doi.org/10.11693/hyhz20190200041
6   X. He, C. Chen, C. Lu, L. Wang, and H. Chen: IOP Conf. Ser.: Earth Environ. Sci. **783** (2021). https://doi.org/10.1088/1755-1315/783/1/012141
7   F. Sun: Marine Sci. Bull. **40** (2021). https://doi.org/10.11840/j.issn.1001-6392.2021.02.013
8   D. Jiang, K. Wang, and Y. Xia: Marine Environ. Sci. **39** (2020). https://doi.org/10.13634/j.cnki.mes.2020.03.021
9   H. Zhang and X. Zheng: J. Ocean Technol. **36** (2017). https://doi.org/10.3969/j.issn.1003-2029.2017.06.002
10 L. Ye, H. Zhang, Z. Zhu, Q. Xu, and Y. Jin: Environ. Sci. Manage. **45** (2020).
11 Y. Li, R. Li, and L. Chang: Ecol. Environ. Sci. **29** (2020). https://doi.org/10.16258/j.cnki.1674-5906.2020.08.013
12 G. Isabella, D. A. Stephen, B. Craig, T. Benjamin, R. Carlton, K. Kohl, and R. R. Nicholas: Ecosphere **10** (2019).
13 M. Izadi, M. Sultan, R. E. Kadiri, A. Ghannadi, and K. Abdelmohsen: Remote Sens. **13** (2021) 3863. https://doi.org/10.3390/rs13193863
14 J. H. Noh, W. Kim, S. H. Son, J. H. Ahn, and Y. J. Park: Harmful Algae **73** (2018) 129. https://doi.org/10.1016/j.hal.2018.02.006
15 L. Ma, Y. Liu, B. Zhang, L. Lu, G. Sun, D. Wang, Z. Liu, B. Li, Y. Wang, Y. Zhang, A. Hu, and X. Yu: Int. J. Remote Sens. **42** (2021) 8661. https://doi.org/10.1080/01431161.2021.1984609
16 D. Jiang and H. Zhang: Marine Sci. **42** (2018). https://doi.org/10.11759/hykx20171215001
17 M.-S. Lee, K.-A. Park, and F. Micheli: Remote Sens. **13** (2021). https://doi.org/10.3390/rs13020298
18 R. Liu, J. Zhang, B. Cui, Y. Ma, P. Song, and J. An: J. Coastal Res. **90** (2019) 120. https://doi.org/10.2112/si90-015.1
19 B. Jiang, H. Li, G. Teng, J. Yan, B. Li, J. Li, X. Zhang, and B. Zhang: J. Zhejiang Univ. (Science Edition) **44** (2017). https://doi.org/10.3785/j.isn.1008-9497.2017.05.013
20 R. Liu, Y. Xiao, Y. Ma, T. Cui, and J. An: ISPRS J. Photogramm. Remote Sens. **184** (2022) 131. https://doi.org/10.1016/j.isprsjprs.2021.12.009
21 Z. Feng, Y. Xuying, S. Xiaoxiao, D. Zhenhong, and L. Renyi: 2018 10th IAPR Workshop on Pattern Recognition in Remote Sensing (PRRS) (2018) 1.
22 P. R. Hill, A. Kumar, M. Temimi, and D. R. Bull: IEEE J. Sel. Top. Appl. Earth Obs. Remote Sens. **13** (2020) 3229. https://doi.org/10.1109/jstars.2020.3001445
23 X. Zhao, R. Liu, Y. Ma, Y. Xiao, J. Ding, J. Liu, and Q. Wang: Remote Sens. **14** (2021). https://doi.org/10.3390/rs14010088
24 Y. Hu, Y. Ma, and J. An: The International Archives of the Photogrammetry, Remote Sensing and Spatial Information Sciences XLII-**3** (2018) 573. https://doi.org/10.5194/isprs-archives-XLII-3-573-2018
25 A. C. Kumar and S. M. Bhandarkar: 2017 IEEE Winter Conf. Applications of Computer Vision (WACV) (2017) 743.
26 S. M. Kim, J. Shin, S. Baek, and J.-H. Ryu: J. Coastal Res. **90** (2019). https://doi.org/10.2112/si90-038.1
27 M.-S. Lee, K.-A. Park, J. Chae, J.-E. Park, J.-S. Lee, and J.-H. Lee: Int. J. Remote Sens. **41** (2019) 5838. https://doi.org/10.1080/01431161.2019.1706011
28 J. Shin, Y. H. Jo, J. H. Ryu, B. K. Khim, and S. M. Kim: Sensors **21** (2021). https://doi.org/10.3390/s21134447